Flame stabilization and pollutant emissions from a H 2 /air dual swirl coaxial injector at elevated pressure

Sylvain Marragou, Dinesh Mengu, Et-Touhami Es-Sebbar, Hervé Magnes, Thierry Schuller, Thibault F Guiberti

Flame stabilization and pollutant emissions from a H_2/air dual swirl coaxial injector at elevated pressure

Sylvain Marragou[a,*], Dinesh Mengu[a], Et-touhami Es-sebbar[a], Hervé Magnes[c], Thierry Schuller[c,d], Thibault F. Guiberti[a,b,**]

[a] *King Abdullah University of Science and Technology (KAUST), Clean Energy Research Platform (CERP), Thuwal, 23955-6900, Saudi Arabia*
[b] *Mechanical Engineering Program, Physical Science and Engineering Division, King Abdullah University of Science and Technology*
[c] *Institut de Mécanique des Fluides de Toulouse, IMFT, Université de Toulouse, CNRS, Toulouse, France*
[d] *Institut Universitaire de France (IUF)*

Abstract

Understanding mechanisms controlling flame stabilization and pollutant emissions in swirled hydrogen flames at elevated pressures is crucial for advancing hydrogen-powered gas turbines. In this work, a single sector model gas turbine combustor operated with a coaxial dual swirl H_2/air injector is installed in a high pressure test rig equipped with optical access. Flame stabilization and pollutant emissions of NO, NO_2, and N_2O are investigated at atmospheric injection temperature across a wide range of air and hydrogen injection velocities and operating pressures up to 8 bars. Two stabilization modes are identified: flames anchored to the hydrogen injector nozzle and flames lifted above the coaxial injector. It is shown that the air injection velocity required to lift the flame from the hydrogen injector rim increases with rising hydrogen velocity or pressure. However, with the current burner design, the lift-off air velocity reaches a plateau beyond 4 bars, regardless of the hydrogen inlet velocity. N_2O emissions remain negligible for all operating conditions explored. Except at very lean operating conditions with global equivalence ratios below 0.3, NO_2 emissions are negligible too. It is finally shown that NO emissions scale with the adiabatic flame temperature, residence time in the flame volume, and pressure and that lifted flames typically yield lower NO emissions than anchored flames. The observations presented in this study help identifying critical flow parameters and lay solid foundations for the development of swirled hydrogen burners at elevated pressures.

Keywords:
Flame shape, NO_x emissions, Hydrogen combustion, High pressure, Injector technology, Gas turbine

*Corresponding author: sylvain.marragou@kaust.edu.sa
**Corresponding author: thibault.guiberti@kaust.edu.sa

1. Introduction

To achieve significant reductions in greenhouse gas emissions and lower NO_x levels, the gas turbine industry considers hydrogen as a promising candidate for replacing hydrocarbon fuels. However, integrating hydrogen into combustion systems also brings new challenges [1–3].

The elevated adiabatic temperature of hydrogen flames, compared to that of hydrocarbons flames at the same equivalence ratio, along with their tendency to burn in diffusion regimes, often results in heightened NO_x emissions and can potentially shorten the lifespan of the combustor [1, 4, 5]. The higher reactivity of hydrogen also introduces additional issues, including a greater risk of flashback, unintended auto-ignition [6], and an increased susceptibility to thermo-acoustic instabilities [2, 5, 7]. A common strategy to reduce the risk of flashback is to delay hydrogen injection until just before it enters the combustion chamber. This approach requires rapid mixing of hydrogen and air to ensure low NO_x emissions and minimize thermal stress on the combustor. This requirement has spurred significant advancements in micro-mixing technologies [8], with the goal of preventing the formation of high-temperature stoichiometric reaction layers at hydrogen injector outlets—well-known contributors to elevated NO_x [9, 10]. Du Toit *et al.* [11] has presented a comprehensive review of various hydrogen-air concepts.

The HYLON injector, which stands for HYdrogen LOw NOx burner, has been developed in recent years [12, 13] with the goal of easy adaptation to existing gas turbine combustion chambers with minimal modifications to current swirled injector technologies. In this coaxial burner, the hydrogen and air streams are both swirled. Initial results demonstrate its promising performance under atmospheric conditions [14, 15] and during high-temperature air injection at atmospheric pressure [16, 17], particularly when flames are stabilized in a lifted regime. This study focuses on assessing the performance of this injector at increased operating pressures.

Yuasa [18] was the first to investigate coaxial dual swirl injection, in which air is introduced through the annular channel and fuel through the central channel. He reported a notable increase in methane flame lift-off; however, achieving flame lift-off for hydrogen proved unsuccessful, even with sonic hydrogen injection. More recently, Degeneve *et al.* [19, 20] investigated dual swirl injection for CH_4/O_2-enriched air flames. Due to the high reactivity of the oxygen-enriched air in the annular channel, the flame remained attached to the central injector lips under all operating conditions when no swirl was conferred to the central fuel injection, irrespective of the swirl intensity in the oxidizer flow.

The HYLON injector uses the same injection scheme, but incorporates a small recess distance of the central injection tube relative to the annular channel outlet. This configuration expands the range of operating conditions that produce lifted flames, reducing NO_x emissions and maintaining the injector lips at a lower temperature. The key parameters controlling flame stabilization have been revealed in [14, 15, 21, 22], but all experiments have been conducted so far at atmospheric pressure.

Multiple NO_x formation mechanisms have been identified for combustion systems, including thermal (Zeldovich), prompt (Fenimore), N_2O, NNH, and pathways involving fuel-bound nitrogen [23–25]. For hydrogen flames, NO_x formation predominantly occurs through the Zeldovich pathway at high temperature for residence time greater than 1 ms [26]. Various mitigation strategies have been implemented to reduce thermal NO_x formation by rapidly cooling the burnt gases right after the combustion zone [27]. Other methods involve diluting the combustion products by injecting air or steam [28, 29] through multiple small holes. NO_x emission levels are primarily influenced by three key parameters: (i) the adiabatic flame temperature [4] (ii) the residence time of the burnt gases in high-temperature zones, typically above 1800 K [27], and (iii) the operating pressure in the combustion chamber [30]. The residence time refers to the duration the gas spend in the flame [31, 32] and is sometimes approximated with the residence time of gas inside the combustion chamber [16, 33, 34]. Only few studies exist on NO_x emissions from H_2/air flames at elevated pressure [3, 29, 35]. They are all very recent and treat the topic of NO_x emissions in a technological point of view by testing several injector designs and evolutions with the goal to minimize NO_x emissions. However, they use NO_x mitigation systems such as air or steam post-combustion dilution and show corrected or dimensionless values, making comparisons difficult.

Experiments at elevated pressures remain scarce but are crucial for the development of future gas turbines fueled with hydrogen. The present study seeks to examine the impact of ambient pressure on flame stabilization and the emissions of NO, NO_2, and N_2O from the HYLON injector. This work represents a significant step forward in evaluating the performance of HYLON injection technology. It lays a foundation for uncovering the mechanisms underlying

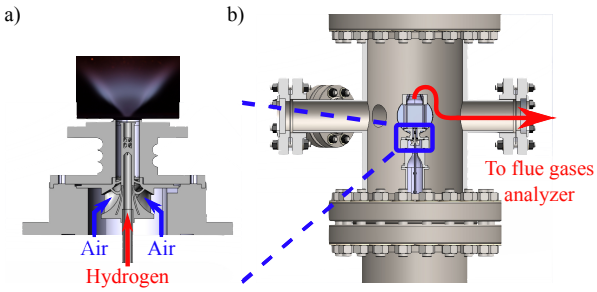

Figure 1: HYLON injector (a) installed in the High Pressure Combustion Duct (HPCD) test bench (b).

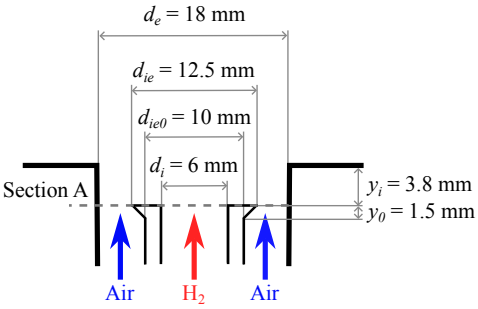

Figure 2: Main dimensions of the HYLON injector used in this study.

flame stabilization and pollutant formation while also highlighting critical directions for future research.

The experimental setup and the diagnostics are described in Section 2. The influence of pressure on flame stabilization is investigated in Section 3. Concentrations of pollutant emissions in the exhaust gases under elevated pressures are then presented and discussed in Section 4. Concluding remarks are provided in Section 5.

2. Experimental setup and methodology

Experiments were conducted with a new version of the HYLON (Hydrogen LOw NOx) injector [14, 15, 21, 22, 34] with a radial to axial swirling vane in the air channel and a beveled lips in an inverted conical shape for the hydrogen injector as the one used in [16] and illustrated in Figs. 1 and 2. It is a H_2/air dual swirl coaxial injector where hydrogen is injected through the central tube and air through the annular tube. The air swirler yields a swirl number of $S_e = 0.9$ estimated from geometrical considerations. The inner swirl number is estimated to be $S_i = 0.6$ with the same considerations. Both swirl motions are in a clockwise direction. The main dimensions of the injector are given in Fig. 2. The inner diameter of the central hydrogen channel is $d_i = 6$ mm and the outer diameter of the annular air channel is $d_e = 18$ mm. The central tube has an initial external diameter of $d_{ie0} = 10$ mm and enlarges linearly in the radial direction to $d_{ie} = 12.5$ mm in the last $y_0 = 1.5$ mm upstream of the outlet of the central hydrogen tube. The outlet of the central hydrogen tube is recessed by $y_i = 3.8$ mm upstream of the outlet of the annular air channel. Downstream of the injector, a square combustion chamber with a close to 360° optical access was installed. The chamber has a length of 145 mm and a width of 78 mm. A converging nozzle from a square to a round section was placed at the top of the combustion chamber with a contraction ratio of 0.51 to avoid the dilution of burnt gases inside the combustion chamber with air entrained from outside the combustor. Figure 1(b) shows the burner equipped with the HYLON injector installed in the HPCD test bench [36]. Bulk velocity values are calculated at section A, as defined by the dimensions indicated in Fig. 2, for an injection temperature fixed to 293 K at the operating pressure p given in absolute values.

The transitions between different flame stabilization regimes were determined according to the flame geometrical criteria described in Section 3. After setting the desired operating conditions, a delay of two minutes of stable operation was maintained to ensure that the system reached thermal steady state. A flame picture was then taken, and the series of flame images were later analyzed according to the specified criteria. The settings of the camera were kept constant for all the pictures. The lower part of the error bars correspond to the steps in injection velocities between each explored operating condition, while the upper part of the error bars are associated with unclear transition conditions. Both upper and lower parts of the error bars account for the repetition of experiments. The determination of the flame stabilization regime was performed during the post-processing of flame pictures based on the flame structure criteria.

A sampling line for the burnt gases was installed in the exhaust, 3 cm upstream of the top of the combustion chamber. The sampled flow was then cooled, dried, and directed to the flue gases analyzer. The concentrations of NO, NO_2, and N_2O were measured using an FTIR (Fourier Transformation Infrared Spectrometer) analyzer (AVL SESAM i60 FT). The measurement uncertainties were experimentally determined. For the minimum detectable concentrations by the FTIR analyzer, the value is determined from the minimum non-zero concentrations detected. They are estimated from gas samples with known concentrations

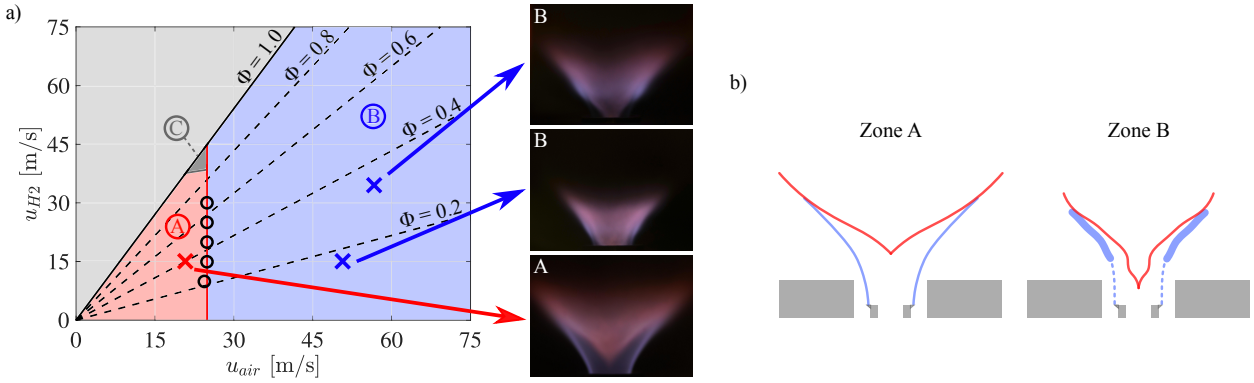

Figure 3: (a) Flame stabilization chart at 1 bar as a function of the air (horizontal axis) and the hydrogen (vertical axis) injection velocities. Black circles correspond to transition from zone A to B. Flame structures are recorded in the visible spectrum. (b) Flame topologies in zone A and B.

of NO, NO_2, and N_2O and with several repetitions of measurements under the same operating conditions. The size of error bars is obtained by adding error bars estimated from measurements with calibration gases and multiple measurement replicates to include both precision and repeatability in the estimation of measurement uncertainties. All concentration measurements presented in the paper are expressed in volumetric ppm, corrected at 15% O_2 to avoid any effects of air dilution on the results.

3. Flame stabilization and structure

The flame stabilization regime above the HYLON injector has a significant impact on pollutant emissions [14]. This injector is similar to the one used by Magnes *et al.* [16] and consequently it shows similar behavior. Two main stabilization regime zones can be identified in Fig. 3.a when the burner is operated at 1 bar. Zone A, characterized by low air injection velocities, corresponds to flames permanently anchored to the central hydrogen injector rim. Zone B, characterized by high air injection velocities, corresponds to flames lifted above the injector. In this regime, the flames can eventually show moments where flame base re-attach to the injector for a very short time, whithout changing the global flame and flow structure. The anchored flames in zone A burn exclusively in diffusion combustion mode, whereas the lifted flames in zone B primarily burn in partially-premixed mode [15, 17]. In the case of lifted flames, diffusion controlled branches correspond to the central reaction front and the tail of external edge flames attempting to propagate to the central injector lips to anchor the flame [22]. In this study, it will be shown that the probability of this observation increases with the operating pressure p. For this injector, and especially at pressures greater than atmospheric, the zone C identified in [34] is very small and not explored in this study. Additionally, the study focuses on globally lean flames, and conditions at global equivalence ratios greater than unity are not explored.

Figure 3.b shows the characteristic topologies of flames in zones A and B. This schematic allows to understand the criteria used to determine the transition from zone A to zone B in the following sections. In zone A, the flame burns entirely in diffusion mode and remains consistently anchored to the central injector lips. The central reaction front (red color) shows a smooth curve and its base is located relatively far from the injector outlet. In this case, the external diffusion reaction front (blue color) separates the hydrogen and air streams. The external and central reaction fronts are well separated up to almost the top of the flame where the two reaction fronts merge. In zone B, the flame is fully or partially lifted above the central injector lips. The central reaction front sits closer to the injector nozzle and the central reaction front alternates with positive and negative curvatures. The external reaction front becomes visually thicker from a mean point of view, typical characteristic of locally premixed flames where the reaction front moves significantly more than in a diffusion reaction front. The separation between the downstream part of the external reaction front and the central reaction front disappears or becomes unclear. In some cases, flames in zone B can alternatively partially re-anchor to the central injector lips (referred here as partially lifted). The suspected key difference between these two stabilization regimes lies in the flow structure, which is modified in the fully anchored flame case (zone A) due to the permanent presence of a hot interface

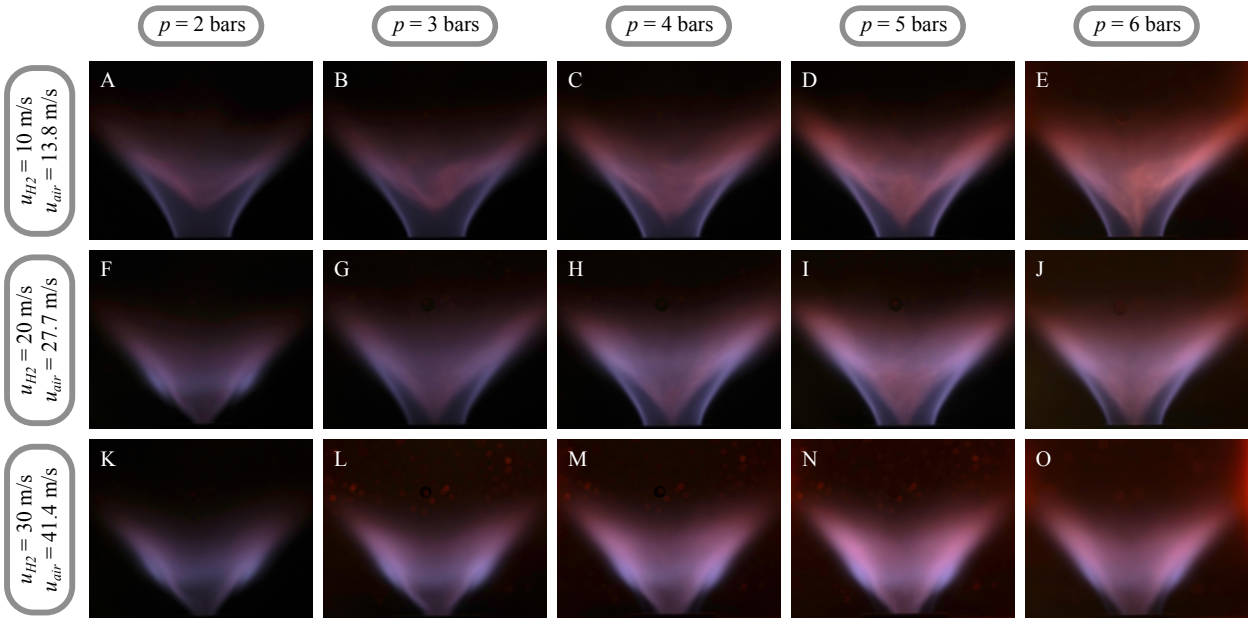

Figure 4: Flame structures recorded in the visible spectrum varying the operating pressure p (horizontal axis) and the hydrogen injection velocity u_{H2} (vertical axis) at constant equivalence ratio $\Phi = 0.4$.

in the external shear layer between the hydrogen and the air streams (the external flame front). This high temperature interface seems to deflect the hydrogen flow to a lower flow angle with respect to the vertical axis, reducing substantially the extent of mixing and increasing the length of the stoichiometric interface. This suspected mechanism will be studied in future work using laser imaging techniques.

Figure 4 shows time-average broadband direct images of flames for some of the explored operating conditions. For these images, the equivalence ratio was fixed at $\Phi = 0.4$. The operating pressure was varied from $p = 2$ to 6 bars (different columns) and the hydrogen injection velocity was varied from $u_{H2} = 10$ to 30 m/s (different rows). For $u_{H2} = 10$ m/s (Figs. 4.A to 4.E), flames are always anchored regardless of the operating pressure between $p = 2$ to 6 bars. The luminosity of the flame increases when the operating pressure increases. Moreover, the base of the central reaction front moves upstream when the operating pressure increases. The diameter and the length of the flame increase slightly with pressure.

When the hydrogen injection velocity is increased to $u_{H2} = 20$ m/s (Figs. 4.F to 4.J), the flame is initially lifted (zone B) in Fig. 4.F at $p = 2$ bars and then shifts to the anchored stabilization regime (zone A) for $p \geq 3$ bars in Fig. 4.G. The central reaction front moves downstream when the flame re-anchors, but then moves upstream when pressure increases further from $p = 3$ to 6 bars.

In the bottom row of Fig. 4, for $u_{H2} = 30$ m/s, flames are always lifted (zone B). Again, the flame luminosity, length, and diameter increase with the operating pressure p. Both blue (in the external reaction front) and red (in the central reaction front) luminous emissions from thermally excited molecules of H_2O^* [37, 38] and $H_2O_2^*$ [38] respectively, are boosted by pressure. The increase in both blue and red intensities is likely due to their common reliance on OH radicals, which help forming $H_2O_2^*$ and H_2O^* excited radicals [38, 39]. Indeed, Fiala and Sattelmayer [38] showed that the intensity of the blue radiation from $H_2O_2^*$ increases with pressure.

Two main behaviors are highlighted when the burner is operated at a constant global equivalence ratio: the flame is more likely to be anchored (zone A) when the pressure p is increased, and more likely to be fully or partially lifted (zone B) when the hydrogen injection velocity u_{H2} is increased. However, the latter observation is primarily related to the fact that the equivalence ratio is fixed, which implies a proportional increase in the air injection velocity u_{air} when the hydrogen injection velocity u_{H2} is increased.

The air injection velocity u_{air} at which the transition from zone A to B occurs is plotted in Fig. 5 against the operating pressure p for different hydrogen injection

Table 1: Operating conditions of the flames presented in the Fig. 4.

Flame	u_{air} [m/s]	u_{H2} [m/s]	p [bars]	Φ	P_{th} [kW]
A			2		5.7
B			3		8.5
C	13.8	10	4	0.4	11.4
D			5		14.2
E			6		17.0
F			2		11.4
G			3		17.0
H	27.8	20	4	0.4	22.7
I			5		28.4
J			6		34.1
K			2		17.0
L			3		25.6
M	41.4	30	4	0.4	34.1
N			5		42.6
O			6		51.1

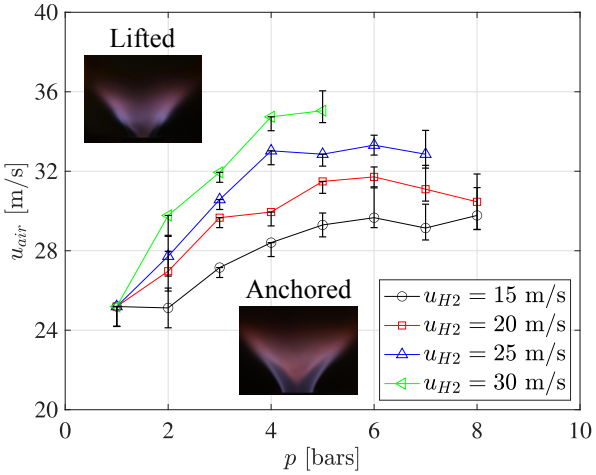

Figure 5: Air injection velocity u_{air} at transition from zone A to zone B plotted against the operating pressure p for different hydrogen injection velocities u_{H2}.

velocities u_{H2}. For each point plotted in Fig. 5, the hydrogen injection velocity and the operating pressure were fixed while the air injection velocity was increased progressively in finite but small steps. Note that for the opposite direction of variation of the air injection velocity, i.e. decreasing it, the transition typically occurs for a slightly lower air injection velocity, but trends are exactly the same. The purpose of Fig. 5 is to determine the minimum air velocity required to transition from an initially anchored flame to a lifted flame, for a given hydrogen injection velocity u_{H2} (i.e. the thermal power) and operating pressure p. At atmospheric pressure ($p = 1$ bar), the hydrogen injection velocity has virtually no-influence on the transition from zone A to B in the range of hydrogen injection velocities u_{H2} explored. For higher operating pressures $p \geq 1$ bar, a clear and consistent behavior appears. Specifically, increasing the hydrogen injection velocity forces the transition from zone A to B to occur at a higher air injection velocity. This is true for all operating pressures $p \geq 2$ bars investigated. Moreover, the air injection velocity at transition increases with the pressure for each hydrogen injection velocity until $p \approx 4$ bars. Above 4 bars, the air injection velocity at transition seems to reach an asymptotic value that depends only on the hydrogen injection velocity. It is difficult to explain the mechanism at the origin of this asymptotic value with previous analysis of HYLON injector and with the limited data on swirl hydrogen flames under elevated pressure. In practical applications, since the goal is to achieve lifted flames which are crucial for reducing NO_x emissions and minimizing thermal stress on injector components, this asymptotic behavior provides reassurance for injector design and helps to define the operating zone of the combustor to ensure lifted flames at all operating pressures.

Previous models developed for flame re-attachment [16, 21, 22] are not applicable for these experiments that focus on flame lift-off. For the following qualitative analysis, it is assumed that the mean flow structure is not significantly altered when the pressure is increased at constant air and

hydrogen injection velocities. As reported in previous studies, the local extinction consecutive to excessive strain of the reaction front can be at the origin of the flame lift-off [40–43]. In this case, the extinction strain rate of diffusion H_2/air flames is the quantity that probably controls the flame lift-off [44]. The observed asymptotic behavior may then result from the non-monotonic behavior of the extinction strain rate in hydrogen/air diffusion flames with pressure, which has been observed experimentally when hydrogen was diluted with nitrogen [45, 46]. Unfortunately, no experimental data are currently available for pure hydrogen on the fuel side due to the complexity of maintaining the necessarily fast flows in the laminar regime. Future work to shed light on stabilization mechanisms of these flames at high-pressure will be carried out and will rely heavily on combined time-resolved laser imaging techniques.

4. Pollutant emissions

Measurements of concentrations of NO, NO_2, and N_2O in the homogeneous exhaust gases are discussed sequentially.

4.1. NO emissions

Figure 6 shows NO concentrations plotted against the hydrogen injection velocity u_{H2} for three different equivalence ratios: $\Phi = 0.2$, 0.4, and 0.6. The corresponding adiabatic flame temperatures T_{ad} are given in Table 2 for atmospheric operating pressure. However, the variation of the adiabatic flame temperature of H_2/air flames over the range of pressure explored in this study is considered as negligible (< 3%). Figure 6.a shows results for an operating pressure of $p = 2$ bars. For $\Phi = 0.2$, the concentration remains below the detectable limit of the FTIR measurement. For higher global equivalence ratios, $\Phi \geq 0.4$, the NO concentration increases with the equivalence ratio and decreases with the hydrogen injection velocity u_{H2}, i.e. the thermal power, which are similar trends as those observed for atmospheric pressure [34]. At the highest hydrogen injection velocities, the NO concentration tends towards an asymptotic value that depends on the global equivalence ratio. For an operating pressure $p = 2$ bars in Fig. 6.a, these values are close to the measurements uncertainties, approximately equal to 3 and 6 ppm at 15% O_2 for equivalence ratios $\Phi = 0.4$ and 0.6 respectively.

Figures 6.a and 6.b show NO emissions at higher pressures of $p = 4$ and 6 bars, respectively. The trends

Table 2: Adiabatic flame temperatures for atmospheric thermodynamic conditions of injection for the different global equivalence ratios Φ investigated in this study.

Φ	T_{ad} [K]
0.2	926
0.4	1426
0.6	1838

of NO concentration as a function of equivalence ratio and hydrogen injection velocity are similar to those observed at 2 bars. At 4 bars, the asymptotic NO concentrations at high hydrogen injection velocities are approximately 6 and 13 ppm at 15% O_2 for equivalence ratios of $\Phi = 0.4$ and $\Phi = 0.6$, respectively. However, at $p = 6$ bars, the experimental setup does not allow for sufficiently high hydrogen injection velocities to determine these asymptotic values. However, the NO concentration increases consistently with the operating pressure p. The NO concentration at low global equivalence ratio $\Phi = 0.2$ remains very low, i.e., under the detection limit of the FTIR, regardless of pressure.

The influence of operating pressure p is further assessed by plotting the measured NO concentration against operating pressure in Fig. 7 for three different equivalence ratios: $\Phi = 0.2$, 0.4, and 0.6. Results for a hydrogen injection velocity of $u_{H2} = 10$ m/s are shown in Fig. 7.a. In this case, all flames are anchored to the central hydrogen injector rim (zone A). For the lowest equivalence ratio $\Phi = 0.2$, NO concentrations remain below the detection limit, except for $p = 8$ bars, where a concentration of 4 ppm is detected. Consistent with Fig. 6, Fig. 7.a shows that the NO concentration increases with operating pressure p. Across the examined pressure range, this increase is nearly linear.

Similar observations are made for a higher hydrogen injection velocity as shown in Fig. 7.b. In this case, all flames with detectable NO concentrations are anchored to the central hydrogen injector rim, except under operating conditions at $\Phi = 0.4$ and $p = 2$ bars and at $\Phi = 0.2$. From $p = 2$ to 4 bars, the evolution of NO concentration with operating pressure p is similar for $\Phi = 0.4$ and 0.6, with an almost linear relationship and slightly lower values for $\Phi = 0.4$. An inflection of the curves starts however to be visible at high pressure for $\Phi = 0.4$, suggesting a possible asymptotic value at high pressure for NO emissions.

For an even higher hydrogen injection velocity, Fig. 7.c shows that all flames with a global equivalence ratio $\Phi \leq 0.4$ are lifted (zone B), while only flames at

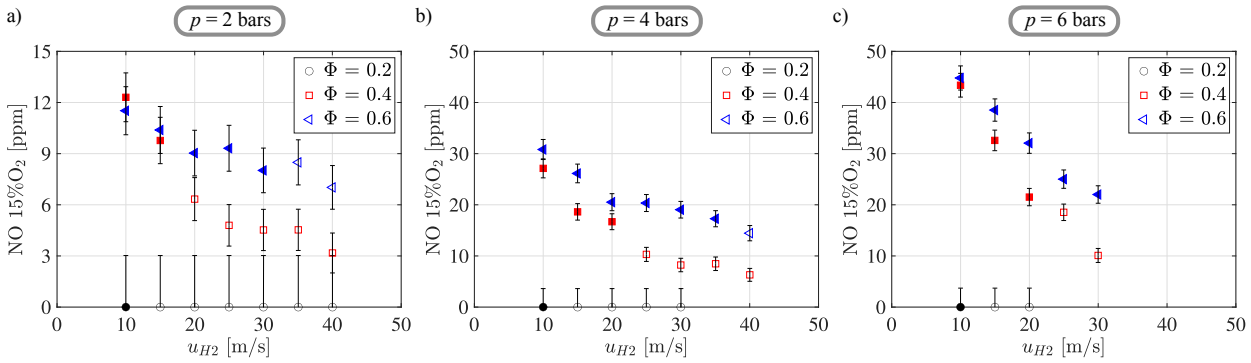

Figure 6: NO concentration measured in the exhaust dry gases plotted against the hydrogen injection velocity u_{H2} for three different equivalence ratios Φ = 0.2, 0.4 and 0.6. (a) p = 2 bars, (b) p = 4 bars, (c) p = 6 bars. Filled symbols: Anchored flames (zone A), Void symbols: Lifted flames (zone B).

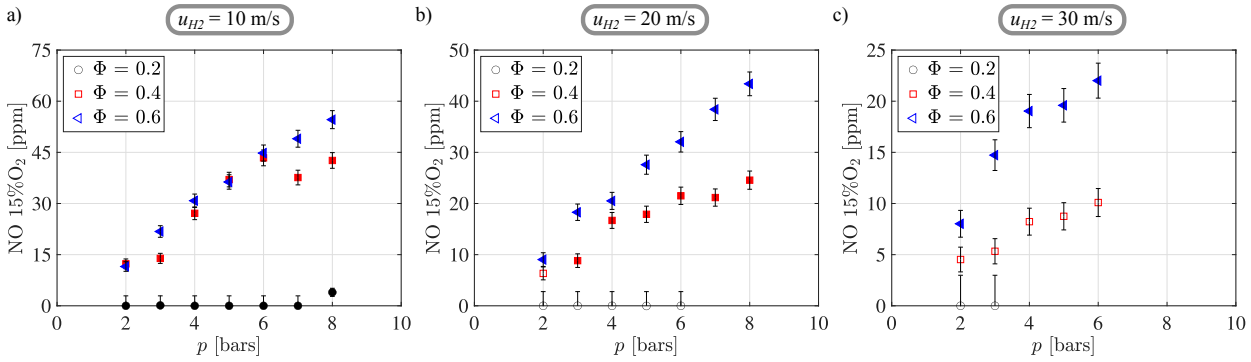

Figure 7: NO concentration measured in the dry exhaust gases plotted against the operating pressure p for three different equivalence ratios Φ = 0.2, 0.4 and 0.6. (a) u_{H2} = 10 m/s, (b) u_{H2} = 20 m/s, (c) u_{H2} = 30 m/s. Filled symbols: Anchored flames (zone A). Void symbols: Lifted flames (zone B).

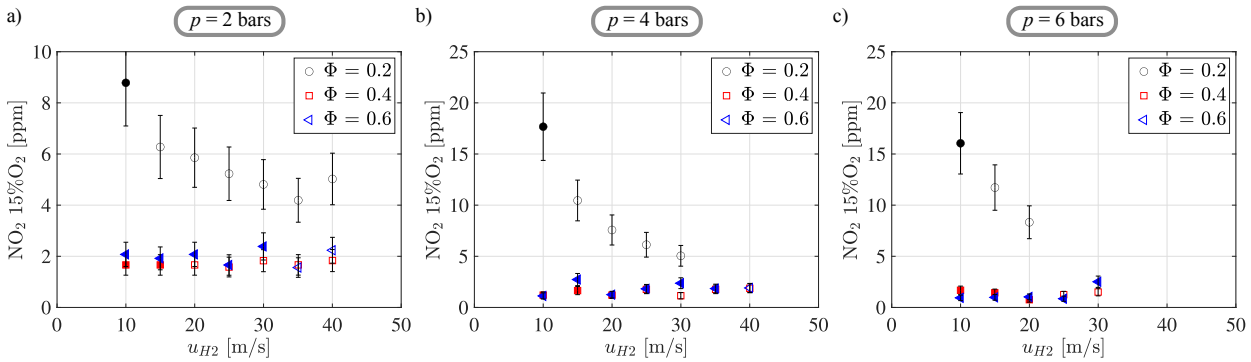

Figure 8: NO_2 concentration measured in the dry exhaust gases plotted against the hydrogen injection velocity u_{H2} for an equivalence ratios Φ = 0.2, 0.4 and 0.6. (a) p = 2 bars, (b) p = 4 bars, (c) p = 6 bars. Filled symbols: Anchored flames (zone A). Void symbols: Lifted flames (zone B).

Φ = 0.6 are anchored (zone A). The NO concentrations for operating points at Φ = 0.2 are still below the detection limit. For this fuel injection velocity of u_{H2} = 30 m/s, the NO concentrations differ for Φ = 0.4 and 0.6 at all pressures. The NO concentration at Φ = 0.4 increases with pressure but with a lower rate compared to Φ = 0.6. This behavior may be due to the different flame stabilization regimes found with Φ = 0.4 (lifted) and Φ = 0.6 (anchored). Consistent with Fig. 6, NO concentrations decrease with an increase in the

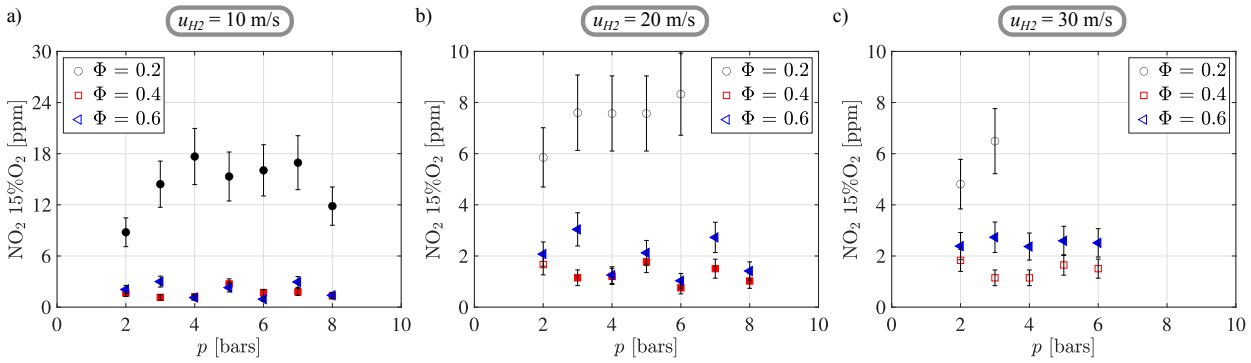

Figure 9: NO_2 concentration measured in the dry exhaust gases plotted against the operating pressure p for an equivalence ratios Φ = 0.2, 0.4 and 0.6. (a) u_{H2} = 10 m/s, (b) u_{H2} = 20 m/s, (c) u_{H2} = 30 m/s. Filled symbols: Anchored flames (zone A). Void symbols: Lifted flames (zone B).

hydrogen injection velocity u_{H2}, regardless of Φ and p. At the highest hydrogen injection velocity tested at u_{H2} = 30 m/s, the inflection of the curves at high pressure becomes more significant, suggesting that at high hydrogen injection velocities, an asymptotic value of NO emissions is reached as the pressure increases. However, the operating conditions achievable with the experimental setup did not allow us to confirm this at higher pressures and/or hydrogen injection velocities, nor to determine the corresponding values.

Figures 6 and 7 show that the lowest NO concentrations are detected at high hydrogen injection velocities, low global equivalence ratios Φ, and low operating pressures p, which generally correspond to the conditions of lifted flames. According to previous studies, NO emissions from H_2/air flames are mainly attributed to the thermal Zeldovich pathway at high temperature for residence time greater than 1 ms [26].. In this case, for a given operating pressure, NO production is primarily controlled by the residence time of burnt gases in the high-temperature zone, typically greater than 1800 K [27]. Therefore, the NO concentration typically increases with the adiabatic flame temperature and the residence time of burnt gases in the flame volume [32, 47] or in the combustion chamber [16, 33, 34]. The operating pressure p, which causes a linear increase in the molecular collision frequency Z, is also known to increase thermal NO formation [30]. For lifted flames (zone B), the distance between the location of hydrogen injection and the flame allows for some premixing, leading to a partially-premixed combustion mode, which may lead to lower thermal NO formation due to the lower flame temperature. However, no clear drop in NO concentrations is detected at the transition from anchored (zone A) to lifted (zone B) flames (see NO emissions for Φ = 0.4 and p = 2, 4, and 6 bars in Figs. 6.a, 6.b, and 6.c), as already noticed in Magnes *et al.* [16]. The low NO concentrations measured at high injection velocities may also be attributed to the shorter residence time of burnt gases in the high-temperature zone. The measured NO concentrations in the exhaust are consistent with NO formation through the thermal Zeldovich pathway.

However, from a technical point of view, it is interesting to note that NO concentrations do not exceed values, typically < 15 ppm at 15% O_2, even at elevated pressure if the hydrogen injection velocity is sufficiently high (typically $u_{H2} \geq$ 25 m/s) and the equivalence ratio is kept relatively low (typically $\Phi \leq$ 0.5). In our upcoming studies, efforts will be made to extend the test bench capabilities and confirm these behaviors at higher flow rates and pressures.

4.2. NO_2 emissions

NO_2 emissions are now examined in Figs. 8 an 9 under the same operating conditions as in Figs. 6 and 7. Among all pressures and hydrogen injection velocities investigated, NO_2 concentrations higher than 3 ppm are measured only at a global equivalence ratio of Φ = 0.2. For this low global equivalence ratio, the measured NO_2 concentrations are greater than NO. This trend have been already observed in a similar setup at atmospheric pressure with a different principle of measurement [17]. It was showed by Hori [48] and Cernansky *et al.* [49] that NO_2 originates from NO oxidation in the turbulent post-combustion mixing region (i.e. the region where burnt gases mix with fresh air) of very fuel-lean and fuel-rich non-perfectly premixed flames. The rate of conversion of NO into NO_2 increases with the initial temperature and the mixing rate of hot burnt gases with fresh air (i.e. the cooling rate). It was also showed

that this mechanism is predominant in zones of low temperature, typically under 1400 K [50]. For $\Phi = 0.4$ and $\Phi = 0.6$, the measured concentrations are almost constant, at approximately 2 ppm. For $p = 2$ bars and $\Phi = 0.2$ (Fig. 8.a) the NO_2 concentration is maximum for the lowest hydrogen injection velocity $u_{H2} = 10$ m/s (anchored flames in zone A) and decreases for higher hydrogen injection velocities (lifted flames in zone B) to reach a plateau at $u_{H2} \approx 30$ m/s. For $p = 4$ and 6 bars (Figs. 8.b and 8.c), the measured NO_2 concentrations for $\Phi = 0.2$ are higher than for $p = 2$ bars. However, for $p = 4$ and 6 bars, the results are very similar and show a decrease without reaching an asymptotic value for high hydrogen injection velocities u_{H2} within the range of velocities explored.

Figure 9 illustrates the influence of operating pressure p on NO_2 emissions for given global equivalence ratios Φ and hydrogen injection velocities u_{H2}. The NO_2 concentrations are plotted against the operating pressure p for three global equivalence ratios: $\Phi = 0.2$, 0.4, and 0.6. Similar to Fig. 8, all measured NO_2 concentrations are between 1 and 2 ppm (i.e. close to the detection limit) for $\Phi = 0.4$ and $\Phi = 0.6$. For anchored flames (zone A) at $\Phi = 0.2$ (Fig. 9.a), NO_2 emissions initially increase with pressure from $p = 2$ to 4 bars and then reach a plateau. At $p = 8$ bars, the measured value is slightly lower than the plateau, but additional measurements at higher pressures would be needed to confirm this trend. With an increase in the hydrogen injection velocity to $u_{H2} = 20$ m/s (Fig. 9.b) the NO_2 emissions for $\Phi = 0.4$ and $\Phi = 0.6$ remain below 3 ppm, similar to Fig. 9.a. For the lowest equivalence ratio $\Phi = 0.2$, all flames are lifted, and NO_2 concentrations are non-negligible. As in Fig. 9.a for $u_{H2} = 10$ m/s, the measured NO_2 concentration in the exhaust burnt gases initially increases with pressure and seems to reach a plateau at around 8 ppm for $p \geq 3$ bars.

Similar trends are observed for $u_{H2} = 30$ m/s in Fig. 9.c but only two operating points could be explored for $\Phi = 0.2$ due to the practical limitations of the experimental bench.

4.3. N_2O emissions

N_2O emissions are reported in Fig. 10. Only the operating conditions with a global equivalence ratio $\Phi = 0.2$ are presented. N_2O concentrations are below the detection limit of the gas analyzer, i.e. ≈ 1 ppm, for $\Phi = 0.4$ and 0.6.

Figure 10.a plots N_2O concentrations as a function of the operating pressure p for three different hydrogen injection velocities $u_{H2} = 10$, 20, and 30 m/s. N_2O emissions are generally very low (below 2.5 ppm) and

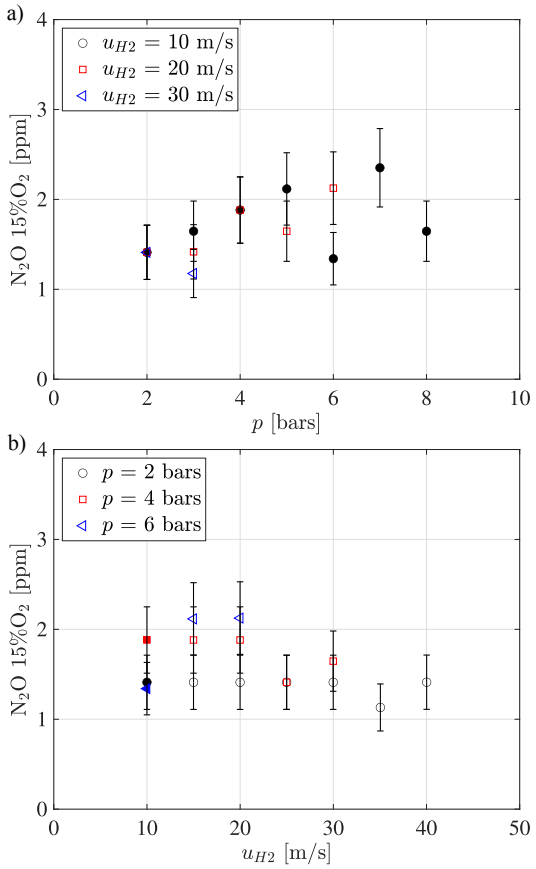

Figure 10: N_2O concentration measured in the dry exhaust gases plotted against the operating pressure p for three different hydrogen injection velocities $u_{H2} = 10$, 20, and 30 m/s (a) and against the hydrogen injection velocities u_{H2} for three different operating pressures $p = 2$, 4, and 6 bars (b). The global equivalence ratio is fixed to $\Phi = 0.2$. Filled symbols: Anchored flames (zone A), Void symbols: Lifted flames (zone B).

seem to globally increase with the operating pressure, although this trend needs further confirmation given the weak pressure sensitivity relative to the size of the error bars.

Additional data are plotted in Fig. 10.b against the hydrogen injection velocity u_{H2} for $p = 2$, 4, and 6 bars. As in Fig. 10.a, all measured concentrations are below 2.5 ppm. Due to the limited data and low values, it is not possible to confidently identify a definitive trend from this dataset. However, the main conclusion is that the N_2O concentration is practically negligible for all the operating conditions explored in this study featuring wide variations of pressures, global equivalence ratios, and hydrogen injection velocities.

4.4. Scaling laws for NO_x emissions

In this section, a scaling law for NO_x concentrations from H_2/air flames is introduced. At high temperature for residence time greater than 1 ms, the primary mechanism for NO_x formation in H_2/air flames follows the Zeldovich pathway [26]. Therefore, NO_x emissions are influenced by the residence time τ_R of burnt gases in the high temperature zone and the flame temperature [4]. The residence time τ_R in the high temperature zone can be defined as the duration over which burnt gases remain either within the combustion chamber [16, 33, 34] or within the flame volume [32, 47]. Both definitions of the residence time are used and compared in this work. In both cases, thermal losses are ignored, and the residence time of gases in a hot zone is calculated taking into account the thermal expansion of gases through the flame and considering bulk flow velocities.

The residence time $\tau_{R,1}$ is calculated from the length of the combustion chamber L_{ch} divided by the mean gas velocity under ambient conditions ($T_0 = 293$ K, $p_0 = p$) in the combustion chamber. The gas velocity is estimated from the total flow rate at the adiabatic flame temperature T_{ad} and the pressure p, divided by the combustion chamber cross-section l_{ch}^2. The values of the adiabatic flame temperatures T_{ad} for the different global equivalence ratios Φ are given in Table 2 for atmospheric operating pressure. The values are obtained using thermodynamic equilibrium calculations performed with Cantera. The weak variation of the adiabatic flame temperature of H_2/air flames with the pressure ($< 3\%$) is neglected in this work. Therefore, the residence time of the flow in the combustion chamber $\tau_{R,1}$ is defined as follows:

$$\tau_{R,1} = \frac{4 L_{ch} l_{ch}^2}{\pi \left(u_e \left(d_e^2 - d_{ie}^2 \right) + u_i d_i^2 \right)} \frac{T_0}{T_{ad}} \qquad (1)$$

The residence time $\tau_{R,2}$ is calculated from the mean flame length L_f divided by the mean gas velocity under ambient conditions. In this case, the cross section of the flow is considered as the area calculated from the diameter d_f at the top of the flame. The flame length l_f and diameter d_f are estimated from time-averaged broadband direct flame images. The residence time of the flow inside the flame volume $\tau_{R,2}$ is then expressed as:

$$\tau_{R,2} = \frac{L_f d_f^2}{\left(u_e \left(d_e^2 - d_{ie}^2 \right) + u_i d_i^2 \right)} \frac{T_0}{T_{ad}} \qquad (2)$$

The starting point is the scaling law $\mathrm{NO}_x \propto T_{ad} \tau_R^{1/3}$, which was already verified for different versions of the HYLON injector in atmospheric conditions [34] and with pre-heated inlet air at atmospheric pressure [16]. The effect of pressure on NO_x concentration is assumed to follow a linear relationship, as the likelihood of thermal NO_x formation is proportional to the molecular collision frequency Z, which increases linearly with pressure p. Consequently, the proposed scaling law is as follows:

$$\mathrm{NO}_x \propto T_{ad} \tau_R^{1/3} p \qquad (3)$$

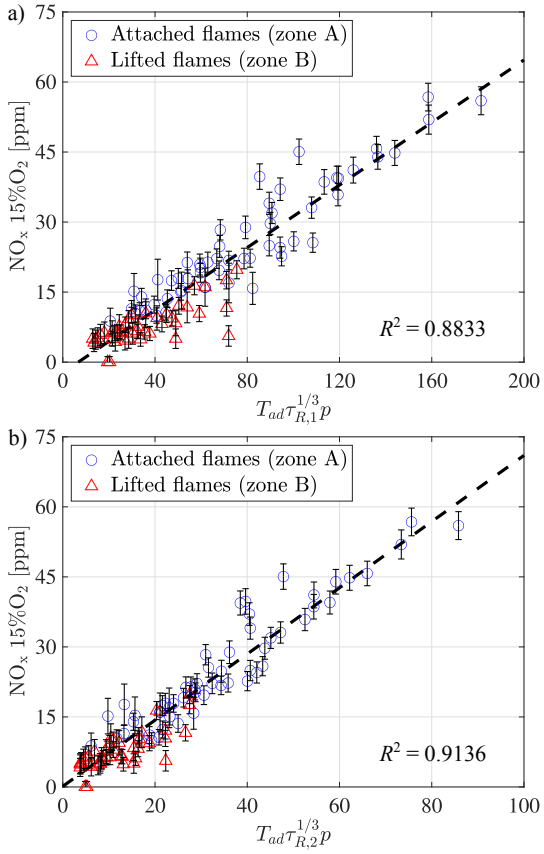

Figure 11: NO_x concentration measured in the homogeneous exhaust gases plotted against the scaling laws based on either the residence time of gases (a) in the combustion chamber or (b) in the flame volume.

Figure 11 shows how NO_x concentrations scale with Eq. (3) by considering the residence time $\tau_{R,1}$ of gases in the combustion chamber defined by Eq. (1) (Fig. 11.a) and the residence time $\tau_{R,2}$ in the mean flame volume defined by Eq. 2 (Fig. 11.b).

In Fig. 11.a, all measured concentrations collapse relatively well around a line with a slope close to

0.335. Most of the data for lifted flames are located at the bottom left side of the figure, while data for anchored flames are at the top right. This indicates that the scaling law accurately reflects the trend of NO_x emissions in relation to adiabatic flame temperature, residence time, and pressure. However, a fraction of the data deviate significantly from the 0.335-slope line and the Y-intercept is slightly below zero, indicating a margin for further improvement in the scaling law. The correlation coefficient derived from the linear fit is $R^2 = 0.88$.

Figure 11.b, obtained with the residence time τ_{R2}, shows a slightly improved collapse of the data around a linear fit with a slope 0.75, which now also cross the zero-origin. The few conditions corresponding to lifted flames that deviate notably from the dashed line in Fig. 11.a are now predicted more accurately by the scaling law. In addition, the measured concentrations for anchored (zone A) and lifted (zone B) flames are now segregated more clearly than in Fig. 11.a. The resulting correlation coefficient increases to $R^2 = 0.91$ confirming the better agreement between the linear fit and the experimental data.

The two approaches show globally reasonable results for the scaling of NO_x emissions. Regardless of the residence time definition, it can be used to estimate NO_x emissions in the exhaust over a wide range of operating conditions, including elevated pressures and requires only a limited amount of input data. Specifically, these input data include only NO_x measurements from a few flames under atmospheric conditions (to calibrate the slope), the combustion chamber width and length, operating pressure, and the inlet flow rates of air and hydrogen, for the case of use of Eq. (1) to estimate the residence time. In the case of use of Eq. (2) yielding the residence time inside the flame volume, flame images are needed trough an optical access to the combustion chamber for the estimation of $\tau_{R,2}$. This second method consequently not allow estimation of NO_x emissions for operating conditions without flame dimensions from experiments or reactive flow simulations. The simplicity and low cost of this method make it a highly useful tool for the preliminary design of hydrogen combustors.

For low hydrogen injection velocities (i.e., low thermal power) and high global equivalence ratios, the NO emissions measured at the exhaust can exceed levels acceptable for real gas turbines. However, this injector has not been optimized for low NO_x emissions, and no NO_x mitigation systems, such as post-combustion air or steam dilution commonly used in real gas turbines, have been applied. Despite the lack of optimization and mitigation systems, the injector is capable of achieving NO_x emission levels of $\leq$ 15 ppm @15% for $\Phi \leq 0.5$ and for pressures greater than 6 bars. Given the measured values of NO_x concentrations at the exhaust, there is significant potential for optimization and mitigation to reduce NO_x emissions, suggesting that this technology is a promising and viable approach for hydrogen-fueled gas turbines with minimal modifications to existing systems. Furthermore, it is challenging to directly compare these results with the limited data available on NO_x emissions from high-pressure H_2/air flames using gas turbine model injectors [3, 29, 35], as these studies often incorporate extensive post-combustion dilution, injector optimization, and sometimes different NO_x correction methods or made dimensionless.

Currently, experiments are underway to precisely understand the mechanisms responsible for NO_x formation with this injection technology, and strategies aimed at reducing NO_x emissions will be proposed based on the findings. For instance, the combustion chamber geometry can be significantly optimized to decrease the residence time of burnt gases. Additionally, dilution systems using fresh air or steam post-combustion can be implemented to substantially lower NO_x concentrations at the exhaust, as is commonly done in real gas turbines.

5. Conclusions

A new version of the H_2/air HYLON injector has been designed and manufactured, and its performance under elevated pressures has been investigated. Specifically, the flame stabilization regimes and the pollutant emissions produced by this injector have been measured and compared at pressures ranging from 1 to 8 bars. As in previous versions of the HYLON injector operated under atmospheric pressure, two main stabilization regimes have been observed: anchored (zone A) and lifted (zone B) flames. Depending on the H_2 and air flow rates adopted, both stabilization regimes were found across all explored pressures.

The main conclusions are:

- The air injection velocity at transition from zone A to zone B increases when the hydrogen injection velocity or the pressure increases. However, for pressures above 4 bars, plateauing occurs and the transition becomes much less sensitive to further pressure increase.
- NO emissions increase when the global equivalence ratio or the pressure increases,

and decrease with the hydrogen injection velocity. At high hydrogen injection velocities, NO_x emissions approach an asymptotic value, which depends on both the global equivalence ratio and the operating pressure.

- Operating conditions leading to lifted flames produce in general lower NO emissions compared to anchored flames.

- Trends of NO_2 emissions with regard to pressure and hydrogen injection velocity are similar to those observed for NO emissions. However, significant NO_2 levels are only found at very low global equivalence ratios, specifically at $\Phi = 0.2$.

- N_2O emissions remain essentially negligible under all operating conditions explored in this study.

- NO_x emissions scale with the adiabatic flame temperature, the pressure, and the residence time of burnt gases in the high temperature zone.

- Two approaches for modeling the residence time, one based on travel through the combustion chamber and the other through the flame volume, have been tested. Both methods provide satisfactory linear fit predictions, with high correlation coefficients close to $R^2 \approx 0.9$. The accuracy is slightly improved when scaling the experimental data using the flame volume. The accuracy is slightly improved when scaling the experimental data using the flame volume. However, this latter approach requires knowledge of the flame dimensions avoiding the estimation of NO_x emissions without flame dimensions obtained from experiments or reactive flow simulations.

This study demonstrates the capability of HYLON technology to achieve low NO_x emissions with lifted H_2/air flames at pressure conditions approaching gas turbine combustor conditions.

Acknowledgements

The research reported in this publication was supported by the King Abdullah University of Science and Technology (KAUST) through a Competitive Research Grant (grant number URF/1/5039–01–01). This work was supported by the KAUST FLEET consortium and its member companies. This project also received funding from European Union Horizon ERC SELECT-H (grant 101097984).

References

[1] P. Chiesa, G. Lozza, L. Mazzocchi, Using hydrogen as gas turbine fuel, Journal of Engineering for Gas Turbines and Power 127 (1) (2005) 73–80.

[2] G. A. Richards, M. M. McMillian, R. S. Gemmen, W. A. Rogers, S. R. Cully, Issues for low-emission, fuel-flexible power systems, Progress in Energy and Combustion Science 27 (2) (2001) 141–169.

[3] C. Clemen, M. Ravikanti, N. La Bianca, R. Eggels, B. Wurm, K. Young, Considerations for Hydrogen Fueled Aerospace Gas Turbine Combustion Sub-System Design, Journal of Engineering for Gas Turbines and Power Volume 3A (2024) V03AT04A016.

[4] O. Tuncer, S. Acharya, J. H. Uhm, Dynamics, NOx and flashback characteristics of confined premixed hydrogen-enriched methane flames, International Journal of Hydrogen Energy 34 (1) (2009) 496–506.

[5] S. Taamallah, K. Vogiatzaki, F. Alzahrani, E. Mokheimer, M. Habib, A. Ghoniem, Fuel flexibility, stability and emissions in premixed hydrogen-rich gas turbine combustion : Technology, fundamentals, and numerical simulations, Applied Energy 154 (2015) 1020–1047.

[6] H. Pers, A. Aniello, F. Morisseau, T. Schuller, Autoignition-induced flashback in hydrogen-enriched laminar premixed burners, International Journal of Hydrogen Energy 48 (27) (2023) 10235–10249. doi:10.1016/j.ijhydene.2022.12.041.

[7] T. Reichel, K. Goeckeler, O. Paschereit, Investigation of lean premixed swirl-stabilized hydrogen burner with axial air injection using OH-PLIF imaging, Journal of Engineering for Gas Turbines and Power 137 (11) (2015) 1–10.

[8] G. Dahl, F. Suttrop, Engine control and low-NOx combustion for hydrogen fuelled aircraft gas turbines, International Journal of Hydrogen Energy 23 (8) (1998) 695–704.

[9] F. Cozzi, A. Coghe, Behavior of hydrogen-enriched non-premixed swirled natural gas flames, International Journal of Hydrogen Energy 31 (6) (2006) 669–677.

[10] J. Oh, J. Hwang, Y. Yoon, EINOx scaling in a non-premixed turbulent hydrogen jet with swirled coaxial air, International Journal of Hydrogen Energy 35 (16) (2010) 8715–8722.

[11] M. H. du Toit, A. V. Avdeenkov, D. Bessarabov, Reviewing H2 combustion: A case study for non-fuel-cell power systems and safety in passive autocatalytic recombiners, Energy & Fuels 32 (6) (2018) 6401–6422.

[12] S. Richard, C. Viguier, S. Marragou, T. Schuller, Dispositif d'injection de dihydrogène et d'air (FR Patent No FR3127988A1), Institut National de la Propriété Industrielle, 2021.

[13] S. Richard, C. Viguier, S. Marragou, T. Schuller, Device for injecting dihydrogen and air (WO Patent No WO2023057722A1), Institut National de la Propriété Industrielle, 2023.

[14] S. Marragou, H. Magnes, T. Poinsot, L. Selle, T. Schuller, Stabilization regimes and pollutant emissions from a dual fuel CH4/H2 and dual swirl low NOx burner, International Journal of Hydrogen Energy 47 (44) (2022) 19275–19288.

[15] A. Aniello, D. Laera, S. Marragou, H. Magnes, L. Selle, T. Schuller, T. Poinsot, Experimental and numerical investigation of two flame stabilization regimes observed in a dual swirl H2-air coaxial injector, Combustion and flame 249 (2023) 112595.

[16] H. Magnes, S. Marragou, A. Aniello, L. Selle, T. Poinsot, T. Schuller, Impact of preheating on flame stabilization and NOx emissions from a dual swirl hydrogen injector, Journal of Engineering for Gas Turbines and Power 146 (5) (2023) 051004.

[17] H. Magnes, M. Vilespy, L. Selle, T. Poinsot, T. Schuller, Interplay Between Unburned Emissions And Nox Emissions From A Dual Swirl Hydrogen Air Injector, Journal of Engineering for Gas Turbines and Power (2024) 1–13.
[18] S. Yuasa, Effects of swirl on the stability of jet diffusion flames, Combustion and Flame 66 (2) (1986) 181–192.
[19] A. Degeneve, C. Mirat, J. Caudal, R. Vicquelin, T. Schuller, Effects of swirl on the stabilization of non-premixed oxygen-enriched flames above coaxial injectors, Journal of Engineering for Gas Turbines and Power 141 (12) (2019) 121018.
[20] A. Degeneve, R. Vicquelin, C. Mirat, J. Caudal, T. Schuller, Impact of co- and counter-swirl on flow recirculation and liftoff of non-premixed oxy-flames above coaxial injectors, Proceedings of the Combustion Institute 38 (4) (2021) 5501–5508.
[21] S. Marragou, H. Magnes, A. Aniello, L. Selle, T. Poinsot, T. Schuller, Experimental analysis and theoretical lift-off criterion for H2/air flames stabilized on a dual swirl injector, Proceedings of the Combustion Institute 39 (4) (2023) 4345–4354.
[22] S. Marragou, H. Magnes, A. Aniello, T. Guiberti, L. Selle, T. Poinsot, T. Schuller, Modeling of H2/air flame stabilization regime above coaxial dual swirl injectors, Combustion and Flame 255 (2023) 112908.
[23] J. Warnatz, U. Maas, R. W. Dibble, Combustion: Physical and chemical fundamentals, modeling and simulation, experiments, pollutant formation, Springer Berlin, Heidelberg, Germany, 1996.
[24] S. R. Turns, Understanding NOx formation in nonpremixed flames: Experiments and modeling, Progress in Energy and Combustion Science 21 (5) (1995) 361–385.
[25] S. C. Li, F. A. Williams, NOx formation in two-stage methane–air flames, Combustion and Flame 118 (3) (1999) 399–414.
[26] A. Konnov, G. Colson, J. De Ruyck, No formation rates for hydrogen combustion in stirred reactors, Fuel 80 (1) (2001) 49–65. doi:10.1016/S0016-2361(00)00060-0.
[27] M. J. Moore, NOx emission control in gas turbines for combined cycle gas turbine plant, Proceedings of the Institution of Mechanical Engineers, Part A: Journal of Power and Energy 211 (1) (1997) 43–52.
[28] S. Göke, C. O. Paschereit, Influence of steam dilution on nitrogen oxide formation in premixed methane/hydrogen flames, Journal of Propulsion and Power 29 (1) (2013) 249–260.
[29] T. Tanneberger, J. Mundstock, C. Rex, S. Rösch, C. O. Paschereit, Development of a Hydrogen Micro Gas Turbine Combustor: NOx Emissions and Secondary Air Injection, Journal of Engineering for Gas Turbines and Power Volume 3A (2024) V03AT04A051.
[30] S. Park, Pressure effect on no emission in methane/air lean-premixed flames, Journal of Mechanical Science and Technology 33 (2019) 3031–3038.
[31] S. R. Turns, F. H. Myhr, R. V. Bandaru, E. R. Maund, Oxides of nitrogen emissions from turbulent jet flames: Part II—Fuel dilution and partial premixing effects, Combustion and Flame 93 (3) (1993) 255–269.
[32] J. Hwang, K. Sohn, N. Bouvet, Y. Yoon, NOx scaling of syngas H2/CO turbulent non-premixed jet flames, Combustion Science and Technology 185 (12) (2013) 1715–1734.
[33] M. Leroy, C. Mirat, A. Renaud, R. Vicquelin, Stabilization of low-NOx hydrogen flames on a dual-swirl coaxial injector, Journal of Engineering for Gas Turbines and Power 145 (2022) 021021.
[34] S. Marragou, Flow structure, mixing, flame stabilization and pollutant emissions from a coaxial dual swirl CH4/H2/air injector, Ph.D. thesis, Université de Toulouse, France (2023). URL https://www.theses.fr/2023INPT0031
[35] M. Overbaugh, V. McDonell, P. Buelow, J. Ryon, B. Williams, O. DeBeni, Design, analysis, and experimental testing of hydrogen lean direct injection nozzles at elevated pressure Volume 3A (2024) V03AT04A074. doi:10.1115/GT2024-126814.
[36] W. R. Boyette, A. M. Elbaz, T. F. Guiberti, W. L. Roberts, Experimental investigation of the near field in sooting turbulent nonpremixed flames at elevated pressures, Experimental Thermal and Fluid Science 105 (2019) 332–341.
[37] R. W. Schefer, W. D. Kulatilaka, B. D. Patterson, T. B. Settersten, Visible emission of hydrogen flames, Combustion and Flame 156 (6) (2009) 1234–1241.
[38] T. Fiala, T. Sattelmayer, Heat release and UV-Vis radiation in non-premixed hydrogen-oxygen flames, Experiments in Fluids 56 (2015) 1–15.
[39] R. W. Schefer, M. Namazian, J. Kelly, Stabilization of lifted turbulent-jet flames, Combustion and Flame 99 (1) (1994) 75–86.
[40] S. Yamaguchi, N. Ohiwa, T. Hasegawa, Structure and blow-off mechanism of rod-stabilized premixed flame, Combustion and Flame 62 (1) (1985) 31–41.
[41] J. Dawson, R. Gordon, J. Kariuki, E. Mastorakos, A. Masri, M. Juddoo, Visualization of blow-off events in bluff-body stabilized turbulent premixed flames, Proceedings of the Combustion Institute 33 (1) (2011) 1559–1566.
[42] A. Palacios, D. Bradley, Generalised correlations of blow-off and flame quenching for sub-sonic and choked jet flames, Combustion and Flame 185 (2017) 309–318.
[43] R. Yuan, J. Kariuki, E. Mastorakos, Measurements in swirling spray flames at blow-off, International Journal of Spray and Combustion Dynamics 10 (3) (2018) 185–210.
[44] Q. An, A. M. Steinberg, The role of strain rate, local extinction, and hydrodynamic instability on transition between attached and lifted swirl flames, Combustion and Flame 199 (2019) 267–278.
[45] C. Sohn, S. Chung, Effect of pressure on the extinction, acoustic pressure response, and NO formation in diluted hydrogen–air diffusion flames, Combustion and Flame 121 (1) (2000) 288–300.
[46] U. Niemann, K. Seshadri, F. Williams, Effect of pressure on structure and extinction of near-limit hydrogen counterflow diffusion flames, Proceedings of the Combustion Institute 34 (1) (2013) 881–886.
[47] S. R. Turns, F. H. Myhr, Oxides of nitrogen emissions from turbulent jet flames: Part I—Fuel effects and flame radiation, Combustion and Flame 87 (3-4) (1991) 319–335.
[48] M. Hori, Nitrogen dioxide formation by the mixing of hot combustion gas with cold air, Symposium (International) on Combustion 22 (1) (1989) 1175–1181.
[49] N. Cernansky, R. Sawyer, NO and NO2 formation in a turbulent hydrocarbon/air diffusion flame, Symposium (International) on Combustion 15 (1) (1975) 1039–1050, fifteenth Symposium (International) on Combustion.
[50] K. Hargeaves, R. Harvey, F. Roper, D. Smith, Formantion of NO2 by laminar flames, Symposium (International) on Combustion 18 (1) (1981) 133–142, eighteenth Symposium (International) on Combustion.